Supplementary Information for

Vacuum Bloch-Siegert Shift in Landau-Polaritons with Ultrahigh Cooperativity

Xinwei Li,[1] Motoaki Bamba,[2] Qi Zhang,[3] Saeed Fallahi,[4] Geoff C. Gardner,[4] Weilu Gao,[1]
Minhan Lou,[1] Katsumasa Yoshioka,[5] Michael J. Manfra,[4,6] and Junichiro Kono[1,7,8,*]

[1]Department of Electrical and Computer Engineering, Rice University,
Houston, Texas 77005, USA,
[2]Department of Material Engineering Science, Osaka University, Osaka 565-0871, Japan,
[3]Argonne National Laboratories, Lemont, Illinois 60439, USA,
[4]Department of Physics and Astronomy, Station Q Purdue, and Birck Nanotechnology Center,
Purdue University, West Lafayette, Indiana 47907, USA,
[5]Department of Physics, Graduate School of Engineering, Yohokama National University,
Yokohama 240-8501, Japan,
[6]School of Materials Engineering and School of Electrical and Computer Engineering,
Purdue University, West Lafayette, Indiana 47907, USA,
[7]Department of Material Science and NanoEngineering, Rice University,
Houston, Texas 77005, USA,
[8]Department of Physics and Astronomy, Rice University, Houston, Texas 77005, USA,

[*]To whom correspondence should be addressed; E-mail: kono@rice.edu.

This PDF file includes:
GaAs quantum wells
Semiclassical simulations
Quantum mechanical theory of Landau polaritons
Asymptotic behavior of the CRA and CRI modes
Determining the values of κ and γ through semiclassical simulations
Minisplittings in experimental spectra
Circularly polarized THz spectroscopy
A comparison with the dynamic BS shift observed in 2D materials

Figures S1-S11
References 1-15

1 GaAs quantum wells

A wafer containing multiple GaAs quantum wells (QWs) was grown by molecular beam epitaxy (MBE). This structure consisted of a total of ten 30-nm-thick GaAs QWs separated by 160 nm $Al_{0.24}Ga_{0.76}As$ barriers. Silicon doping layers were placed at 80 nm setback within $Al_{0.24}Ga_{0.76}As$ barriers. The growth temperature was $635°C$, but it was decreased to $450°C$ for the deposition of the silicon atoms to minimize the diffusion of donors. An electron density per QW of 3.2×10^{11} cm^{-2} and a mobility of 8.8×10^6 cm^2/Vs were extracted from Hall measurements at 300 mK in the dark. The total electron density of the multiple QW structure was 3.2×10^{12} cm^{-2}. Figure S1 shows conduction band bottom and electron density profiles for the studied structure simulated using the nextnano software package [1].

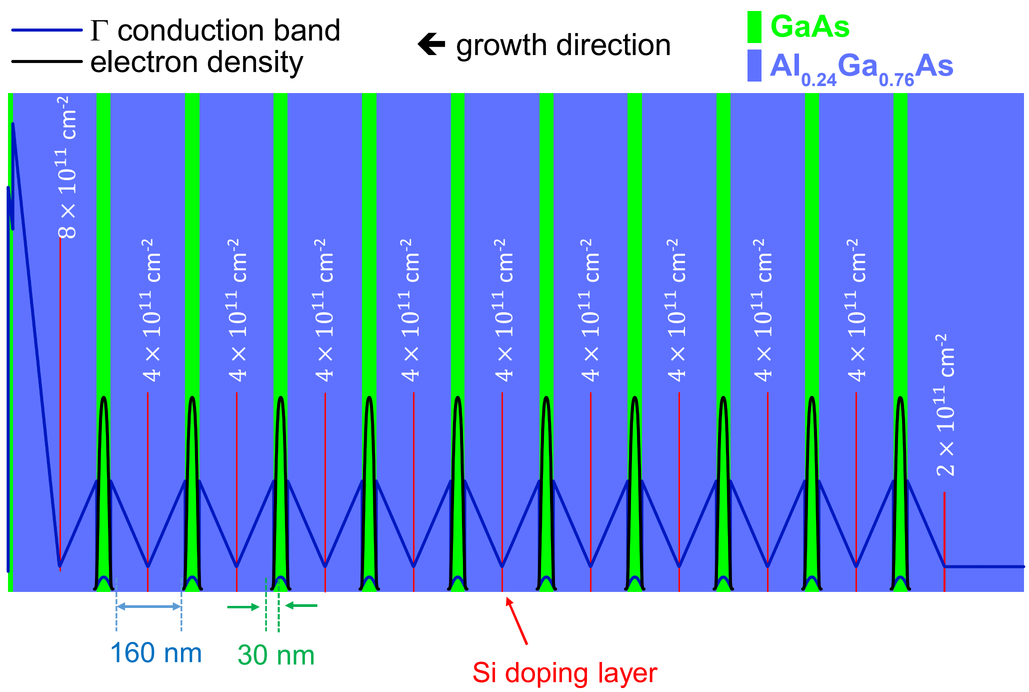

Figure S1: Simulated conduction band bottom and electron density profiles of the multiple QW structure.

2 Semiclassical simulations

2.1 Transfer-matrix method

Since our 1D photonic-crystal cavity (PCC) integrated with the multiple QW structure had translational symmetry within the sample x-y plane (z is along the Bragg mirror stacking direction, i.e., the multiple QW growth direction), we were able to use the transfer-matrix method (TMM) to reproduce experimental transmission spectra [2]. For an electromagnetic wave normal incident onto an isotropic multilayer structure, the complex transmission coefficient t and reflection coefficient r satisfy:

$$\begin{pmatrix} t \\ 0 \end{pmatrix} = Q \begin{pmatrix} 1 \\ r \end{pmatrix}. \tag{S1}$$

Here, Q is the 2 by 2 transfer matrix calculated from cascading multiplications of the matrices of the different layers

$$Q = M_{N,N-1} \cdot P_{N-1}(d_N - 1) \cdot M_{N-1,N-2} ... M_{2,1} \cdot P_1(d_1) \cdot M_{1,0} \ , \tag{S2}$$

where M and P represent an interface matrix and a propagation matrix, respectively, d is the layer thickness, and subscripts are layer indexes that range from 0 to N. t and r can be calculated by $t = Q_{11} - (Q_{12}Q_{21}/Q_{22})$, and $r = -Q_{21}/Q_{22}$, and the power transmittance and reflectance are $T = |t|^2$ and $R = |r|^2$, respectively.

Material parameters enter Eq. (S2) through the refractive index of the N-th layer n_N in the M and P matrices:

$$M_{N,N-1} = \frac{1}{2} \begin{pmatrix} 1 + n_{N-1}/n_N & 1 - n_{N-1}/n_N \\ 1 - n_{N-1}/n_N & 1 + n_{N-1}/n_N \end{pmatrix} \tag{S3}$$

$$P_N = \begin{pmatrix} e^{i n_N \frac{\omega}{c} d_N} & 0 \\ 0 & e^{-i n_N \frac{\omega}{c} d_N} \end{pmatrix} \tag{S4}$$

We used $n_{\text{Si}} = 3.4$ for silicon and $n_0 = 1$ for the vacuum spacings. For the 2DEG layer, we first calculated the DC surface conductivity from the expression $\sigma_{\text{DC}} = ne\mu$, where n is the total surface electron density and $\mu = e\tau/m^*$ is the electron mobility. The elements of the Drude conductivity tensor of the 2DEG in a perpendicular magnetic field are given by

$$\sigma_{xx} = \frac{\sigma_{\text{DC}}(1 - i\omega\tau)}{(1 - i\omega\tau)^2 + (\omega_c\tau)^2}, \ \sigma_{xy} = -\frac{\sigma_{\text{DC}}\omega_c\tau}{(1 - i\omega\tau)^2 + (\omega_c\tau)^2}. \tag{S5}$$

In the circular polarization basis, the conductivity eigenvalues for the CR-active and CR-inactive polarization modes, respectively, are expressed as

$$\sigma_{\text{CRA}} = \sigma_{xx} + i\sigma_{xy} = \frac{\sigma_{\text{DC}}}{1 - i(\omega - \omega_c)\tau}, \; \sigma_{\text{CRI}} = \sigma_{xx} - i\sigma_{xy} = \frac{\sigma_{\text{DC}}}{1 - i(\omega + \omega_c)\tau}. \tag{S6}$$

The bulk dielectric permittivity and refractive index of the 2DEG layer for the CRA and CRI polarization modes are then calculated as

$$\varepsilon_{\text{CRA}} = \varepsilon_{\text{bg}} + i\sigma_{\text{CRA}}/(\varepsilon_0 \omega d_{\text{QW}}), \; \varepsilon_{\text{CRI}} = \varepsilon_{\text{bg}} + i\sigma_{\text{CRI}}/(\varepsilon_0 \omega d_{\text{QW}}). \tag{S7}$$

$$n_{\text{CRA}} = (\varepsilon_{\text{CRA}})^{1/2}, \; n_{\text{CRI}} = (\varepsilon_{\text{CRI}})^{1/2}, \tag{S8}$$

where we chose the background dielectric permittivity $\varepsilon_{\text{bg}} = 3.6^2$ to be the same as GaAs, and d_{QW} is the total thickness of the multiple QW membrane.

The above material parameters, combined with experimental cavity structure parameters such as layer thicknesses and separations, allowed us to calculate transmission spectra as a function of magnetic field; see Fig. 3 in the main text. Excellent agreement between simulation and experimental data was achieved without any adjustable fitting parameter.

3 Quantum mechanical theory of Landau polaritons

3.1 Hamiltonian

We have developed a quantum mechanical model starting from the Maxwell equations and the Newton equation of charged particles experiencing the Lorentz force. Below, we show how we derived a quantum Hamiltonian from these fundamental classical mechanical equations, using a standard quantization procedure [3].

The equation of motion for the position $\boldsymbol{r}_j$ of the j-th charged particle with mass m_j and charge e_j is expressed as

$$m_j \ddot{\boldsymbol{r}}_j = e_j \boldsymbol{E}(\boldsymbol{r}_j) + e_j \dot{\boldsymbol{r}}_j \times \boldsymbol{B}(\boldsymbol{r}_j). \tag{S9}$$

Here, the dot "$\dot{}$" means the time derivative, and $\boldsymbol{E}(\boldsymbol{r})$ and $\boldsymbol{B}(\boldsymbol{r})$ are the vectors of the electric field and the magnetic flux density, respectively. The Maxwell equations involving these fields are expressed with the charge density $\rho(\boldsymbol{r}) \equiv$

$\sum_j e_j \delta(\boldsymbol{r} - \boldsymbol{r}_j)$ and the electric current density $\boldsymbol{J}(\boldsymbol{r}) \equiv \sum_j e_j \dot{\boldsymbol{r}}_j \delta(\boldsymbol{r} - \boldsymbol{r}_j)$ as

$$\nabla \cdot \boldsymbol{E}(\boldsymbol{r}) = \rho(\boldsymbol{r})/\varepsilon_0, \tag{S10a}$$

$$\nabla \cdot \boldsymbol{B}(\boldsymbol{r}) = 0, \tag{S10b}$$

$$\nabla \times \boldsymbol{E}(\boldsymbol{r}) = -\dot{\boldsymbol{B}}(\boldsymbol{r}), \tag{S10c}$$

$$\nabla \times \boldsymbol{B}(\boldsymbol{r}) = \mu_0 \boldsymbol{J}(\boldsymbol{r}) + \dot{\boldsymbol{E}}(\boldsymbol{r})/c^2. \tag{S10d}$$

Here, ε_0, μ_0, and c are the permittivity, permeability, and speed of light in vacuum, respectively. Following the standard quantization procedure [3], in the Coulomb gauge, we get the so-called minimal-coupling Hamiltonian

$$\hat{H} = \int \mathrm{d}\boldsymbol{r} \left[\frac{\varepsilon_0 \hat{\boldsymbol{E}}_\perp(\boldsymbol{r})^2}{2} + \frac{\hat{\boldsymbol{B}}(\boldsymbol{r})^2}{2\mu_0} \right] + \sum_j \frac{[\hat{\boldsymbol{p}}_j - e_j \hat{\boldsymbol{A}}(\hat{\boldsymbol{r}}_j)]^2}{2m_j} + V(\{\hat{\boldsymbol{r}}_j\}). \tag{S11}$$

Here, the first and second terms are the energies of the transverse electric field $\hat{\boldsymbol{E}}_\perp(\boldsymbol{r})$ and the magnetic flux density $\hat{\boldsymbol{B}}(\boldsymbol{r})$, respectively. The latter is represented with the vector potential $\hat{\boldsymbol{A}}(\boldsymbol{r})$ as $\hat{\boldsymbol{B}}(\boldsymbol{r}) = \nabla \times \hat{\boldsymbol{A}}(\boldsymbol{r})$. On the other hand, the former is expressed as $\hat{\boldsymbol{E}}_\perp(\boldsymbol{r}) = -\boldsymbol{\Pi}(\boldsymbol{r})/\varepsilon_0$, where $\boldsymbol{\Pi}(\boldsymbol{r})$ is the conjugate momentum of the vector potential satisfying $[\hat{\boldsymbol{A}}(\boldsymbol{r}), \hat{\boldsymbol{\Pi}}(\boldsymbol{r})] = \mathrm{i}\hbar \boldsymbol{\delta}_\perp(\boldsymbol{r} - \boldsymbol{r}')$. Here, $\boldsymbol{\delta}_\perp(\boldsymbol{r})$ is the transverse delta function tensor [3]. The last term in Eq. (S11) represents the Coulomb interaction depending on the particles' positions $\{\hat{\boldsymbol{r}}_j\}$, and the second last term is the kinetic energy for particle velocity $[\hat{\boldsymbol{p}}_j - e_j \hat{\boldsymbol{A}}(\hat{\boldsymbol{r}}_j)]/m_j$, where $\hat{\boldsymbol{p}}_j$ is the conjugate momentum of $\hat{\boldsymbol{r}}_j$ satisfying $[\hat{\boldsymbol{r}}_j, \hat{\boldsymbol{p}}_{j'}] = \mathrm{i}\hbar \delta_{j,j} \mathbf{1}$.

From the minimal-coupling Hamiltonian, Eq. (S11), we next derive the Hamiltonian in the main text by making some approximations. First, we separate the charged particles into the two-dimensional electron gas (2DEG) and those composing the background dielectric media, i.e., the photonic-crystal cavity (PCC). When we can neglect the frequency dependence of the background relative permittivity $\varepsilon_{\mathrm{cav}}(\boldsymbol{r})$, we need not explicitly consider the degrees of freedom of the background charged particles, but their influence can be considered by simply replacing the vacuum permittivity ε_0 with $\varepsilon_0 \varepsilon_{\mathrm{cav}}(\boldsymbol{r})$ [4] as

$$\hat{H} \approx \hat{H}_{\mathrm{cav}} + \sum_{j=1}^{N} \frac{[\hat{\boldsymbol{p}}_j + e \hat{\boldsymbol{A}}(\hat{\boldsymbol{r}}_j)]^2}{2m^*} + V'(\{\hat{\boldsymbol{r}}_j\}), \tag{S12}$$

where

$$\hat{H}_{\mathrm{cav}} = \int \mathrm{d}\boldsymbol{r} \left[\frac{\varepsilon_0 \varepsilon_{\mathrm{cav}}(\boldsymbol{r}) \hat{\boldsymbol{E}}_\perp(\boldsymbol{r})^2}{2} + \frac{\hat{\boldsymbol{B}}(\boldsymbol{r})^2}{2\mu_0} \right]. \tag{S13}$$

Now, the 2DEG consists of N electrons with charge $-e$ and effective mass m^*. The effective-mass approximation is valid here, since the electrons in our sample move only near the bottom of the conduction band. While the Coulomb interaction $V'(\{\hat{\boldsymbol{r}}_j\})$ is modified from that in Eq. (S11), thanks to Konh's theorem [5], we do not have to consider electron-electron interactions in the following calculations, since we discuss only the linear optical response.

We consider that the 1D THz PCC (including the substrate and background medium of the 2DEG layer) is described by a z-dependent relative permittivity $\varepsilon_{\text{cav}}(z)$. For simplicity, we consider only the photonic and polariton modes with no in-plane wavevector, and the electromagnetic fields depend only on z. The transverse electromagnetic fields are in the x-y plane. The external static magnetic flux density $\boldsymbol{B}_{\text{s}}$, applied in the z direction, is treated to be constant in the following calculations. The cavity photon Hamiltonian is expressed as

$$\hat{H}_{\text{cav}} = \int \mathrm{d}\boldsymbol{r} \left[\frac{\varepsilon_0 \varepsilon_{\text{cav}}(z) \hat{\boldsymbol{E}}(z)^2}{2} + \frac{\hat{\boldsymbol{B}}(z)^2}{2\mu_0} \right] \tag{S14}$$

$$= \int \mathrm{d}\boldsymbol{r} \left[\frac{\hat{\boldsymbol{\Pi}}(z)^2}{2\varepsilon_0 \varepsilon_{\text{cav}}(z)} + \frac{1}{2\mu_0} \left(\frac{\partial}{\partial z} \hat{\boldsymbol{A}}(z) \right)^2 \right]. \tag{S15}$$

The magnetic flux density $\hat{\boldsymbol{B}}(z) = \nabla \times \hat{\boldsymbol{A}}(z)$ is represented by the vector potential $\hat{\boldsymbol{A}}(z)$. The electric field $\hat{\boldsymbol{E}}(z) = -\hat{\boldsymbol{\Pi}}(z)/[\varepsilon_0 \varepsilon_{\text{cav}}(z)]$ is represented by the conjugate momentum $\hat{\boldsymbol{\Pi}}(z)$ of the vector potential, which satisfies $[\hat{A}_\xi(z), \hat{\Pi}_{\xi'}(z')] = \mathrm{i}\hbar \delta_{\xi,\xi'} \delta(z - z')/S$ for $\xi, \xi' = x, y$, where S is an area of the x-y plane.

We assume that the 2DEG is located at z_{2DEG} in the z direction, and the electrons move freely in the x-y plane. In the long-wavelength approximation, and omitting the electron-electron Coulomb interaction, the total Hamiltonian given by Eq. (S12) is rewritten as

$$\hat{H} \approx \hat{H}_{\text{cav}} + \sum_{j=1}^{N} \frac{[\hat{\boldsymbol{\pi}}_j + e\hat{\boldsymbol{A}}(z_{\text{2DEG}})]^2}{2m^*}, \tag{S16}$$

where $N = nS$ is the number of electrons for surface density n and area S, m^* is the electron effective mass, and $\hat{\boldsymbol{\pi}}_j \equiv \hat{\boldsymbol{p}}_j + e\boldsymbol{A}_0$ is the in-plane momentum of the j-th electron with the static vector potential $\boldsymbol{A}_0$, with the external magnetic flux density being $\boldsymbol{B}_{\text{s}} = \nabla \times \boldsymbol{A}_0$. Introducing $\hat{\pi}_\pm \equiv (\hat{\pi}_x \mp \mathrm{i}\pi_y)/\sqrt{2}$ and the lowering operator $\hat{c} \equiv (\hat{\pi}_y + \mathrm{i}\hat{\pi}_x)/\sqrt{2m^*\hbar\omega_{\text{c}}} = \mathrm{i}\hat{\pi}_+/\sqrt{m^*\hbar\omega_{\text{c}}}$ between the Landau levels satisfying $[\hat{c}, \hat{c}^\dagger] = 1$ [6], we can rewrite the Hamiltonian as

$$\hat{H} = \hat{H}_{\text{cav}} + \sum_{j=1}^{N} \frac{\hat{\boldsymbol{\pi}}_j{}^2}{2m^*} + \frac{e}{m^*} \sum_{j=1}^{N} \hat{\boldsymbol{\pi}}_j \cdot \hat{\boldsymbol{A}}(z_{\text{2DEG}}) + \frac{Ne^2}{2m^*} \hat{\boldsymbol{A}}(z_{\text{2DEG}})^2 \tag{S17a}$$

$$= \hat{H}_{\text{cav}} + \sum_{j=1}^{N} \frac{\hat{\boldsymbol{\pi}}_j{}^2}{2m^*} + \frac{e}{m^*} \sum_{j=1}^{N} \left[\hat{\pi}_{j,-} \hat{A}_+(z_{\text{2DEG}}) + \hat{A}_-(z_{\text{2DEG}}) \hat{\pi}_{j,+} \right]$$
$$+ \frac{Ne^2}{m^*} \hat{A}_-(z_{\text{2DEG}}) \hat{A}_+(z_{\text{2DEG}}) \tag{S17b}$$

$$= \hat{H}_{\text{cav}} + \sum_{j=1}^{N} \hbar\omega_{\text{c}} \left(\hat{c}_j^\dagger \hat{c}_j + \frac{1}{2} \right) + \mathrm{i} \sqrt{\frac{\hbar\omega_{\text{c}} e^2}{m^*}} \sum_{j=1}^{N} \left[\hat{c}_j^\dagger \hat{A}_+(z_{\text{2DEG}}) - \hat{A}_-(z_{\text{2DEG}}) \hat{c}_j \right]$$
$$+ \frac{Ne^2}{m^*} \hat{A}_-(z_{\text{2DEG}}) \hat{A}_+(z_{\text{2DEG}}). \tag{S17c}$$

The second term is the energy of the electron cyclotron motion with frequency $\omega_{\text{c}} = eB/m^*$. The third term contains the lowering and raising processes by the non-Hermitian vector potential

$$\hat{A}_\pm(z) \equiv \frac{\hat{A}_x(z) \mp \mathrm{i}\hat{A}_y(z)}{\sqrt{2}}. \tag{S18}$$

The last term is the so-called A^2 (or diamagnetic) term.

Let us quantize the electromagnetic wave in the medium with relative permittivity $\varepsilon_{\text{cav}}(z)$, following Ref. [7]. Hamilton's equations are obtained from Eq. (S15) for the $\xi = x, y$ components as

$$\frac{\partial}{\partial t} A_\xi(z,t) = \frac{\partial \hat{H}_{\text{cav}}}{\partial \Pi_\xi} = \frac{\Pi_\xi(z,t)}{\varepsilon_0 \varepsilon_{\text{cav}}(z)}, \tag{S19a}$$

$$\frac{\partial}{\partial t} \Pi_\xi(z,t) = -\frac{\partial \hat{H}_{\text{cav}}}{\partial A_\xi} = \frac{1}{\mu_0} \frac{\partial^2}{\partial z^2} A_\xi(z,t). \tag{S19b}$$

Then, we can reproduce the wave equation for the vector potential in the frequency domain as

$$\frac{\partial^2}{\partial z^2} A_\xi(z,\omega) + \frac{\omega^2}{c^2} \varepsilon_{\text{cav}}(z) A_\xi(z,\omega) = 0. \tag{S20}$$

The eigen-functions and eigen-frequencies of this wave equation correspond to the modes of the electromagnetic wave in the medium. However, instead of Eq. (S20), here we consider the following wave equation for $f_{n_z}(z) \propto \sqrt{\varepsilon_{\text{cav}}(z)} A_\xi(z)$:

$$\frac{1}{\sqrt{\varepsilon_{\text{cav}}(z)}} \frac{\partial^2}{\partial z^2} \frac{f_{n_z}(z)}{\sqrt{\varepsilon_{\text{cav}}(z)}} + \frac{(\omega_{\text{cav}}^{n_z})^2}{c^2} f_{n_z}(z) = 0. \tag{S21}$$

Here, $\omega_{\text{cav}}^{n_z}$ is the eigen-frequency corresponding to the eigen-function $f_{n_z}(z)$. We normalize $f_{n_z}(z)$ as

$$\int \mathrm{d}z \; f_{n_z}(z)^* f_{n'_z}(z) = \delta_{n_z, n'_z}. \tag{S22}$$

We can also show the following completeness:

$$\sum_{n_z} f_{n_z}(z)^* f_{n_z}(z') = \delta(z - z'). \tag{S23}$$

For simplicity, here we assume that all the eigen-functions $\{f_{n_z}(z)\}$ are real functions. We can basically make real eigen-functions from the complex eigen-functions if $\varepsilon_{\text{cav}}(z)$ is a real function (for example, in vacuum, two propagating waves $\mathrm{e}^{\pm \mathrm{i}(\omega/c)z}$ can be transformed into real functions $\sin[(\omega/c)z]$ and $\cos[(\omega/c)z]$). From the complete set of the eigen-functions and eigen-frequencies, we describe the operators of the vector potential and its conjugate momentum as

$$\hat{A}_\xi(z) = \sum_{n_z} \sqrt{\frac{\hbar}{2\varepsilon_0 \varepsilon_{\text{cav}}(z) \omega_{\text{cav}}^{n_z} S}} f_{n_z}(z) \left(\hat{a}_{n_z,\xi}^\dagger + \hat{a}_{n_z,\xi} \right), \tag{S24a}$$

$$\hat{\mathit{\Pi}}_\xi(z) = \sum_{n_z} \mathrm{i} \sqrt{\frac{\varepsilon_0 \varepsilon_{\text{cav}}(z) \hbar \omega_{\text{cav}}^{n_z}}{2S}} f_{n_z}(z) \left(\hat{a}_{n_z,\xi}^\dagger - \hat{a}_{n_z,\xi} \right). \tag{S24b}$$

Here, $\hat{a}_{n_z,\xi}$ is the annihilation operator of a photon in the n_z-th cavity mode with polarization in the ξ direction, satisfying

$$\left[\hat{a}_{n_z,\xi}, \hat{a}_{n'_z,\xi'}^\dagger \right] = \delta_{n_z,n'_z} \delta_{\xi,\xi'}. \tag{S25}$$

We can check that Eqs. (S24a) and (S24b) certainly satisfy $[\hat{A}_\xi(z), \hat{\mathit{\Pi}}_{\xi'}(z')] = \mathrm{i}\hbar \delta_{\xi,\xi'} \delta(z - z')/S$. Equation (S24a) also satisfies the wave equation, Eq. (S20). The Hamiltonian, Eq. (S15), can now be rewritten as

$$\begin{aligned} \hat{H}_{\text{cav}} &= \sum_{\xi=x,y} \sum_{n_z} \frac{\hbar \omega_{\text{cav}}^{n_z}}{4} \left[\left(\hat{a}_{n_z,\xi}^\dagger + \hat{a}_{n_z,\xi} \right)^2 - \left(\hat{a}_{n_z,\xi}^\dagger - \hat{a}_{n_z,\xi} \right)^2 \right] \\ &= \sum_{\xi=x,y} \sum_{n_z} \hbar \omega_{\text{cav}}^{n_z} \left(\hat{a}_{n_z,\xi}^\dagger \hat{a}_{n_z,\xi} + \frac{1}{2} \right). \end{aligned} \tag{S26}$$

In general, in addition to these cavity modes (localized mode), there are also continuous modes (transmission modes).

The non-Hermitian vector potential defined in Eq. (S18) does not correspond to the circularly polarized field, which should be expressed as a Hermitian operator as

$$\hat{A}_{\pm}^{\text{circ}}(z) = \sum_{n_z} \sqrt{\frac{\hbar}{2\varepsilon_0 \varepsilon_{\text{cav}}(z) \omega_{\text{cav}}^{n_z} S}} f_{n_z}(z) \left(\hat{a}_{n_z,\pm}^{\dagger} + \hat{a}_{n_z,\pm} \right), \tag{S27}$$

where the annihilation operator is defined as

$$\hat{a}_{n_z,\pm} \equiv \frac{\hat{a}_{n_z,x} \mp \mathrm{i} \hat{a}_{n_z,y}}{\sqrt{2}}. \tag{S28}$$

In terms of these annihilation operators, the non-Hermitian vector potential, Eq. (S18), is expressed as

$$\hat{A}_{\pm}(z) = \sum_{n_z} \sqrt{\frac{\hbar}{2\varepsilon_0 \varepsilon_{\text{cav}}(z) \omega_{\text{cav}}^{n_z} S}} f_{n_z}(z) \left(\hat{a}_{n_z,\mp}^{\dagger} + \hat{a}_{n_z,\pm} \right). \tag{S29}$$

Here, we introduce an annihilation operator $\hat{b}$ of a collective excitation of cyclotron motion as

$$\hat{b} \equiv \frac{1}{\sqrt{N}} \sum_{j=1}^{N} \hat{c}_j. \tag{S30}$$

This operator describes the collective motion excited by the electromagnetic field in the long-wavelength approximation, while there exist other collective motions with different amplitudes for different electrons. In fact, we should in principle consider the Landau levels occupied by the electrons and the coupling enhancement by a factor $\sqrt{\nu+1}$ at the ν-th level. However, as far as the linear optical response is concerned, the following Hamiltonian gives the same results. In terms of $\hat{b}$ and $\hat{a}_{n_z,\pm}$, the total Hamiltonian, Eq. (S17c), is rewritten as

$$\begin{aligned}
\hat{H} = &\sum_{\xi=\pm} \sum_{n_z} \hbar \omega_{\text{cav}}^{n_z} \left(\hat{a}_{n_z,\xi}^{\dagger} \hat{a}_{n_z,\xi} + \frac{1}{2} \right) + \hbar \omega_{\text{c}} \left(\hat{b}^{\dagger} \hat{b} + \frac{1}{2} \right) \\
&+ \sum_{n_z} \mathrm{i} \hbar \bar{g}_{n_z} \left[\hat{b}^{\dagger} (\hat{a}_{n_z,+} + \hat{a}_{n_z,-}^{\dagger}) - \hat{b} (\hat{a}_{n_z,-} + \hat{a}_{n_z,+}^{\dagger}) \right] \\
&+ \sum_{n_z,n_z'} \frac{\hbar \bar{g}_{n_z} \bar{g}_{n_z'}}{\omega_{\text{c}}} (\hat{a}_{n_z,-} + \hat{a}_{n_z,+}^{\dagger}) (\hat{a}_{n_z',+} + \hat{a}_{n_z',-}^{\dagger}),
\end{aligned} \tag{S31}$$

where the interaction strength at the cyclotron frequency $\omega_{\rm c}$ for mode n_z is represented, with the background relative permittivity $\varepsilon_{\rm bg} = \varepsilon_{\rm cav}(z_{\rm 2DEG})$ of the active layer, as

$$\bar{g}_{n_z} = \sqrt{\frac{e^2\omega_{\rm c} n}{2\varepsilon_0\varepsilon_{\rm bg} m^* \omega_{\rm cav}^{n_z}}} f_{n_z}(z_{\rm 2DEG}). \tag{S32}$$

We can define an effective cavity length as $L_{n_z} = 2/|f_{n_z}(z_{\rm 2DEG})|^2$ so that Eq. (S32) can be written as

$$\bar{g}_{n_z} = \sqrt{\frac{e^2\omega_{\rm c} n}{\varepsilon_0\varepsilon_{\rm bg} m^* \omega_{\rm cav}^{n_z} L_{n_z}}}. \tag{S33}$$

Equation (S31) is the full Hamiltonian given in the main text as Eq. (1). As seen in the second line of Eq. (S31), the cyclotron resonance (CR) excitation interacts with the "+" circularly polarized photons in the co-rotating manner ($\hat{b}^\dagger \hat{a}_{n_z,+}$ and $\hat{b}\hat{a}_{n_z,+}^\dagger$), while it interacts with the "$-$" circularly polarized photons in the counter-rotating manner ($\hat{b}^\dagger \hat{a}_{n_z,-}^\dagger$ and $\hat{b}\hat{a}_{n_z,-}$).

When we focus on the first cavity mode ($n_z = 1$), the eigen-frequencies of the system are obtained by solving the equations of motion for the full Hamiltonian. For the "+" and "$-$" modes, the eigen-frequencies are found, respectively, from

$$\omega^3 - \omega_{\rm c}\omega^2 - \omega_{\rm cav}^1 \left(\omega_{\rm cav}^1 + \frac{2\bar{g}_1{}^2}{\omega_{\rm c}}\right)\omega + \omega_{\rm c}(\omega_{\rm cav}^1)^2 = 0 \ , \tag{S34a}$$

$$\omega^3 + \omega_{\rm c}\omega^2 - \omega_{\rm cav}^1 \left(\omega_{\rm cav}^1 + \frac{2\bar{g}_1^2}{\omega_{\rm c}}\right)\omega - \omega_{\rm c}(\omega_{\rm cav}^1)^2 = 0 \ . \tag{S34b}$$

In Fig. S2, we plot the eigen-frequencies of the system calculated by Eq. (S34) as a function of magnetic flux density B. For "+" circularly polarized light (the CRA mode), we get the VRS feature, as plotted by the blue solid lines. For "$-$" circularly polarized light (the CRI mode), we get the vacuum BS shift, as plotted by the red solid line. This result is similar to what was observed experimentally.

Below, we verify that the above results are not changed when we consider the multiple transitions between Landau levels in the case of fractional electron filling. The degeneracy in each Landau level *per spin* is given by $N_L = BS/\Phi_0$, where $\Phi_0 = h/e$ is the magnetic flux quantum. The total number of electrons is $N = nS$, and the filling factor is $\nu = N/(2N_L) = n\Phi_0/(2B)$, where the factor of 2 is from the spin degree of freedom. Then, each Landau level is filled by $2N_L$ electrons, and the Landau levels ($\ell = 0, 1, 2, \ldots$) are occupied up to $\ell_f \equiv \lfloor \nu \rfloor$. In general, the ℓ_f-th level is partially occupied by $2(\nu - \ell_f)N_{\rm L}$ electrons, and the lower levels

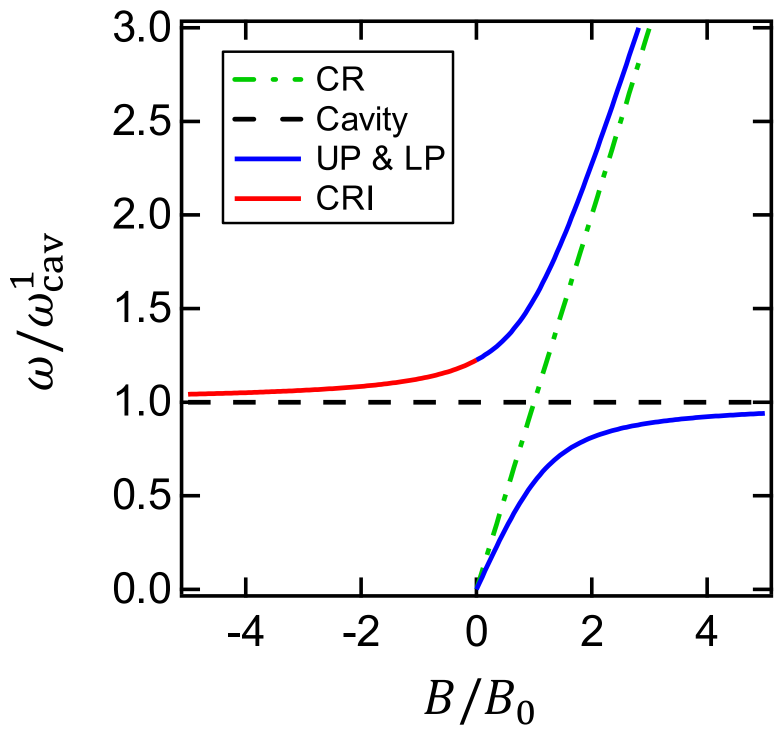

Figure S2: Polariton dispersions calculated using a full quantum mechanical model considering only the first-order cavity mode for the $g_1/\omega^1_{\text{cav}} = 0.5$ case. B_0 is the static magnetic field at zero detuning.

($\ell < \ell_f$) are fully occupied. Then, there are two possible transitions for weak enough light irradiation. One is the $\ell_f \to (\ell_f + 1)$ transition, involving $2(\nu - \ell_f)N_{\text{L}}$ electrons. Considering the $\sqrt{\ell_f + 1}$-times enhancement factor ($\hat{c}^\dagger|\ell_f\rangle = \sqrt{\ell_f + 1}|\ell_f + 1\rangle$), the interaction strength for this collective excitation is

$$\bar{g}_{n_z,\ell_f+1} = \frac{\bar{g}_{n_z}}{\sqrt{N}}\sqrt{2(\nu - \ell_f)N_{\text{L}}}\sqrt{\ell_f + 1} = \bar{g}_{n_z}\sqrt{\frac{(\nu - \ell_f)(\ell_f + 1)}{\nu}}. \tag{S35}$$

The other is the $(\ell_f - 1) \to \ell_f$ transition, involving $2N_{\text{L}} - 2(\nu - \ell_f)N_{\text{L}}$ electrons (the number of unoccupied electron states in the ℓ_f-th level). Considering the $\sqrt{\ell_f}$-times enhancement, the interaction strength for this collective excitation is

$$\bar{g}_{n_z,\ell_f} = \frac{\bar{g}_{n_z}}{\sqrt{N}}\sqrt{2(1 - \nu + \ell_f)N_{\text{L}}}\sqrt{\ell_f} = \bar{g}_{n_z}\sqrt{\frac{(1 - \nu + \ell_f)\ell_f}{\nu}}. \tag{S36}$$

Then, the total Hamiltonian given by Eq. (S31) is rewritten as

$$\hat{H} = \sum_{\xi=\pm}\sum_{n_z} \hbar\omega_{n_z}\left(\hat{a}^\dagger_{n_z,\xi}\hat{a}_{n_z,\xi} + \frac{1}{2}\right) + \sum_{\ell=\ell_f}^{\ell_f+1} \hbar\omega_{\mathrm{c},\ell}\hat{b}^\dagger_\ell \hat{b}_\ell$$
$$+ \sum_{\ell=\ell_f}^{\ell_f+1}\sum_{n_z} \mathrm{i}\hbar\bar{g}_{n_z,\ell}\left[\hat{b}^\dagger_\ell(\hat{a}_{n_z,+} + \hat{a}^\dagger_{n_z,-}) - \hat{b}_\ell(\hat{a}_{n_z,-} + \hat{a}^\dagger_{n_z,+})\right]$$
$$+ \sum_{n_z,n'_z} \frac{\hbar\bar{g}_{n_z}\bar{g}_{n'_z}}{\omega_\mathrm{c}}(\hat{a}_{n_z,-} + \hat{a}^\dagger_{n_z,+})(\hat{a}_{n'_z,+} + \hat{a}^\dagger_{n'_z,-}). \tag{S37}$$

Here, $\hat{b}_\ell$ is the annihilation operator of a collective excitation between the $(\ell-1)$-th and ℓ-th Landau levels. $\omega_{\mathrm{c},\ell}$ is its transition frequency, and it can be modified from ω_c when the non-parabolicity of the band is non-negligible [8]. However, a realistic estimate of the non-parabolicity of the conduction band in our GaAs QW suggests that our Landau-polariton frequencies change very little, and it is in fact negligible in our system ($\omega_{\mathrm{c},\ell} \approx \omega_\mathrm{c}$). In this approximation, by considering the multiple Landau level transitions, Eqs. (S34) are rewritten as

$$\omega^3 \mp \omega_\mathrm{c}\omega^2 - \omega^1_\mathrm{cav}\left(\omega^1_\mathrm{cav} + \sum_{\ell=\ell_f}^{\ell_f+1}\frac{2\bar{g}_{1,\ell}{}^2}{\omega_\mathrm{c}}\right)\omega \pm \omega_\mathrm{c}(\omega^1_\mathrm{cav})^2 = 0. \tag{S38}$$

However, after simple calculations using Eqs. (S35) and (S36), Eq. (S38) reduces exactly to Eqs. (S34). Then, the effective refractive index in Eqs. (3) and (4) in the main text is also not changed. In this way, even when we consider the multiple transitions between the Landau levels, our Landau-polariton frequencies are not changed for small enough non-parabolicity and weak enough THz radiation.

3.2 Interaction strength

By the transfer-matrix method, we calculated transmission and reflection spectra for the cavity without a 2DEG, which allowed us to estimate the resonance frequency $\omega^{n_z}_\mathrm{cav}$ of the n_z-th cavity mode. Then, we calculated the electric field $E(z)$ inside the cavity for a monochromatic incident wave with frequency $\omega^{n_z}_\mathrm{cav}$. The operator of the electric field is expressed as

$$\hat{E}_\xi(z) = -\frac{\hat{\Pi}_\xi(z)}{\varepsilon_0\varepsilon_\mathrm{cav}(z)} = -\mathrm{i}\sum_k \sqrt{\frac{\hbar\omega^{n_z}_\mathrm{cav}}{2\varepsilon_0\varepsilon_\mathrm{cav}(z)S}} f_{n_z}(z)\left(\hat{a}^\dagger_{n_z,\xi} - \hat{a}_{n_z,\xi}\right). \tag{S39}$$

Then, the shape of the n_z-th eigen-function $f_k(z)$ is determined as

$$f_{n_z}(z) \propto \sqrt{\varepsilon_{\text{cav}}(z)} E_{n_z}(z). \tag{S40}$$

In our estimation, we normalize the wave function by its amplitude inside the cavity:

$$\int_{\text{inside cavity}} \mathrm{d}z \, |f_{n_z}(z)|^2 = 1. \tag{S41}$$

Here, the inside also includes the Si layers comprising the photonic crystal cavity. The outside of the cavity is considered as photonic reservoirs, by which the photonic loss is introduced in the cavity quantum electrodynamics calculation. In the estimation of the interaction strength, we do not need to consider the photonic reservoir (outside the cavity). The absolute value of $f_{n_z}(z_{\text{2DEG}})$ is determined in this way.

The interaction strength $\bar{g}_{n_z}$ in Eq. (S32) depends on ω_{c}, which changes with the external magnetic field B in the experiment. Here, we define a ω_{c}-independent interaction strength as

$$g_{n_z} = \sqrt{\frac{e^2 n}{2\varepsilon_0 \varepsilon_{\text{bg}} m^*}} f_{n_z}(z_{\text{2DEG}}) = \sqrt{\frac{\omega_{\text{cav}}^{n_z}}{\omega_{\text{c}}}} \bar{g}_{n_z}. \tag{S42}$$

In other words, g_{n_z} is the interaction strength at zero detuning ($\omega_{\text{cav}}^{n_z} = \omega_{\text{c}}$). From the parameters n, m^*, ε_{bg} (determined for reproducing the transmittance spectra), and $f_{n_z}(z_{\text{2DEG}})$ determined by the transfer-matrix method for lowest mode in the empty cavity, we obtained the interaction strength $g_1/2\pi = 0.15$ THz between the first cavity mode and CR.

3.3 Spectra with and without the counter-rotating and A^2 terms

As mentioned in the main text, to elucidate quantitative contributions from the counter-rotating terms (CRTs) and the A^2 terms in the full Hamiltonian, we calculated polariton spectra while selectively switching on and off these terms.

For now, we only consider the $n_z = 1$ photonic mode. Based on the full Hamiltonian, Eq. (S31), and using the same notations as in Eq. (S34), we derived the modified Hamiltonians and polariton dispersion equations for both circularly polarized modes ("±") for a total of four cases. The results are listed below, and the corresponding polariton dispersions are plotted in Fig. S3.

1. With CTs and A^2 terms

$$\hat{H} = \hbar\omega_{\mathrm{c}}\hat{b}^\dagger\hat{b} + \mathrm{i}\hbar\bar{g}_1\left[\hat{b}^\dagger(\hat{a}_+ + \hat{a}_-^\dagger) - (\hat{a}_- + \hat{a}_+^\dagger)\hat{b}\right] + \frac{\hbar\bar{g}_1{}^2}{\omega_{\mathrm{c}}}(\hat{a}_- + \hat{a}_+^\dagger)(\hat{a}_+ + \hat{a}_-^\dagger) + \sum_{\xi=\pm}\hbar\omega_{\mathrm{cav}}\hat{a}_\xi^\dagger\hat{a}_\xi. \tag{S43}$$

$$\omega^3 \mp \omega_{\mathrm{c}}\omega^2 - \omega_{\mathrm{cav}}\left(\omega_{\mathrm{cav}} + \frac{2\bar{g}_1^2}{\omega_{\mathrm{c}}}\right)\omega \pm \omega_{\mathrm{c}}\omega_{\mathrm{cav}}{}^2 = 0 \tag{S44}$$

2. With CRTs but without A^2 terms

$$\hat{H} = \hbar\omega_{\mathrm{c}}\hat{b}^\dagger\hat{b} + \mathrm{i}\hbar\bar{g}_1\left[\hat{b}^\dagger(\hat{a}_+ + \hat{a}_-^\dagger) - (\hat{a}_- + \hat{a}_+^\dagger)\hat{b}\right] + \sum_{\xi=\pm}\hbar\omega_{\mathrm{cav}}^1\hat{a}_\xi^\dagger\hat{a}_\xi. \tag{S45}$$

$$\omega^3 \mp \omega_{\mathrm{c}}\omega^2 - (\omega_{\mathrm{cav}}^1)^2\omega \mp (2\bar{g}_1^2\omega_{\mathrm{cav}}^1 - (\omega_{\mathrm{cav}}^1)^2\omega_{\mathrm{c}}) = 0 \tag{S46}$$

3. Without CRTs but with A^2 terms

$$\hat{H} = \hbar\omega_{\mathrm{c}}\hat{b}^\dagger\hat{b} + \mathrm{i}\hbar\bar{g}_1(\hat{b}^\dagger\hat{a}_+ - \hat{a}_+^\dagger\hat{b}) + \frac{\hbar\bar{g}_1{}^2}{\omega_{\mathrm{c}}}(\hat{a}_+^\dagger\hat{a}_+ + \hat{a}_-^\dagger\hat{a}_-) + \sum_{\xi=\pm}\hbar\omega_{\mathrm{cav}}^1\hat{a}_\xi^\dagger\hat{a}_\xi. \tag{S47}$$

$$\omega_+ = \frac{\omega'_{\mathrm{cav}} + \omega_{\mathrm{c}}}{2} \pm \sqrt{\frac{(\omega'_{\mathrm{cav}} - \omega_{\mathrm{c}})^2}{4} + \bar{g}_1^2} \tag{S48}$$

$$\omega_- = \omega'_{\mathrm{cav}} \tag{S49}$$

$$\omega'_{\mathrm{cav}} = \omega_{\mathrm{cav}}^1 + \frac{\bar{g}_1^2}{\omega_{\mathrm{c}}} = \omega_{\mathrm{cav}}^1 + \frac{g_1{}^2}{\omega_{\mathrm{cav}}} \tag{S50}$$

4. Without CRTs and without A^2 terms

$$\hat{H} = \hbar\omega_{\mathrm{c}}\hat{b}^\dagger\hat{b} + \mathrm{i}\hbar\bar{g}_1(\hat{b}^\dagger\hat{a}_+ - \hat{a}_+^\dagger\hat{b}) + \sum_{\xi=\pm}\hbar\omega_{\mathrm{cav}}^1\hat{a}_\xi^\dagger\hat{a}_\xi. \tag{S51}$$

$$\omega_+ = \frac{\omega_{\mathrm{cav}}^1 + \omega_{\mathrm{c}}}{2} \pm \sqrt{\frac{(\omega_{\mathrm{cav}}^1 - \omega_{\mathrm{c}})^2}{4} + \bar{g}_1^2} \tag{S52}$$

$$\omega_- = \omega_{\mathrm{cav}}^1 \tag{S53}$$

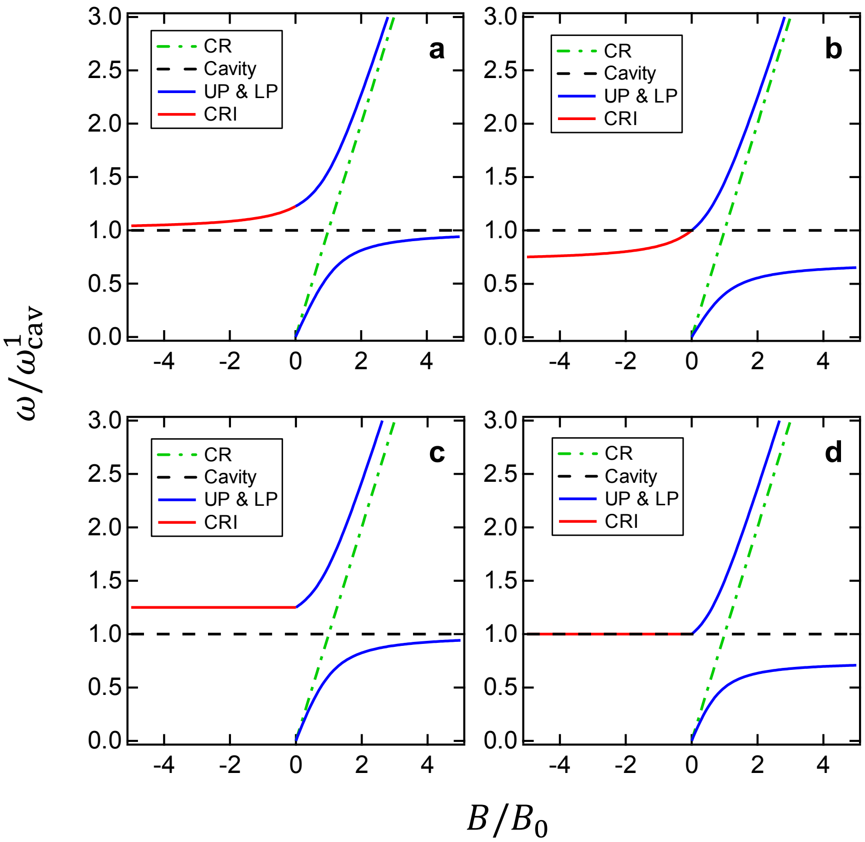

Figure S3: Polariton dispersions calculated from four Hamiltonians where CRTs and A^2 terms are selectively dropped. **a**, Full Hamiltonian. **b**, with the CRTs but without the A^2 terms. **c**, without the CRTs but with the A^2 terms. **d**, without the CRTs and without the A^2 terms. B_0 is the static magnetic field at zero detuning. $g_1/\omega^1_{\text{cav}} = 0.5$.

In order to perform realistic theoretical calculations to compare with the experiment, considering only the $n_z = 1$ photonic mode is not sufficient, so we combined semiclassical simulations with the quantum mechanical theory described above. Here, we show the procedure for simulating the transmittance spectra without the contributions from the CRTs and from the A^2 terms.

From the total Hamiltonian, Eq. (S17b), Hamilton's equation for $\hat{\Pi}_\xi$ is derived in the presence or absence of the A^2 term (last term in Eq. (S17b)) as

$$\frac{\partial}{\partial t}\mathit{\Pi}_\pm(z,t) = \frac{1}{\mu_0}\frac{\partial^2}{\partial z^2}A_\pm(z,t) - \frac{e}{m^* S}\sum_{j=1}^{N}\begin{cases}[\pi_{j,\pm}(t)+eA_\pm(z,t)] & \text{(with } A^2 \text{ term).}\\ \pi_{j,\pm}(t) & \text{(without } A^2 \text{ term).}\end{cases} \tag{S54}$$

Then, the wave equation, Eq. (S20), is rewritten by the presence of the 2DEG as

$$\frac{\partial^2}{\partial z^2}A_\pm(z,\omega) + \frac{\omega^2}{c^2}\varepsilon_{\text{cav}}(z)A_\pm(z,\omega) = -\mu_0 J_\pm(\omega). \tag{S55}$$

Here, the current density is defined with or without the photonic contribution of the electrons' momentum, depending on the presence of the A^2 term as

$$J_\pm(\omega) = -\frac{e}{m^* S}\sum_{j=1}^{N}\begin{cases}[\pi_{j,\pm}(t)+eA_\pm(z,t)] & \text{(with } A^2 \text{ terms).}\\ \pi_{j,\pm}(t) & \text{(without } A^2 \text{ terms).}\end{cases} \tag{S56}$$

On the other hand, in the classical treatment of light, the non-Hermitian vector potential in the Hamiltonian is expanded by the amplitude $A_\pm(\omega)$ with the $\pm$ circular polarization as

$$A_\pm(t) = \int_0^\infty \mathrm{d}\omega\, [\mathrm{e}^{\mathrm{i}\omega t}A_\mp(\omega)^* + \mathrm{e}^{-\mathrm{i}\omega t}A_\pm(\omega)]. \tag{S57}$$

The first and second terms, respectively, correspond to those in Eq. (S29). From the Hamiltonian, Eq. (S17b), we get the following relation from the equation of motion of $\pi_{j,\pm}$ (the coefficient corresponds to the Green's function in the linear response theory):

$$\pi_{j,\pm}(\omega) = \frac{\pm e\omega_{\mathrm{c}}}{\omega \mp \omega_{\mathrm{c}} + \mathrm{i}0^+}A_\pm(\omega). \tag{S58}$$

In this way, the CRA $(+)$ circular polarization interacts with CR in the co-rotating manner as $\pi_{j,+} \propto A_+/(\omega-\omega_{\mathrm{c}})$, which arises from the co-rotating terms $\hat{b}^\dagger\hat{a}_{n_z,+}$ and $\hat{b}\hat{a}^\dagger_{n_z,+}$ in Eq. (S31). On the other hand, the CRI $(-)$ circular polarization interacts with CR in the counter-rotating manner as $\pi_{j,-} \propto A_-/(\omega+\omega_{\mathrm{c}})$, which arises from the counter-rotating terms (CRTs) $\hat{b}^\dagger\hat{a}^\dagger_{n_z,-}$ and $\hat{b}\hat{a}_{n_z,-}$ in Eq. (S31). Then, depending on the presence of the CRTs, Eq. (S58) is rewritten as

$$\pi_{j,+}(\omega) = \frac{e\omega_{\mathrm{c}}}{\omega - \omega_{\mathrm{c}} + \mathrm{i}0^+}A_+(\omega). \tag{S59a}$$

$$\pi_{j,-}(\omega) = \begin{cases}\dfrac{-e\omega_{\mathrm{c}}}{\omega+\omega_{\mathrm{c}}+\mathrm{i}0^+}A_+(\omega) & \text{(with CRTs).}\\ 0 & \text{(without CRTs).}\end{cases} \tag{S59b}$$

Finally, the optical conductivity $\sigma_\pm(\omega) = J_\pm(\omega)/E_\pm(\omega) = J_\pm(\omega)/[\mathrm{i}\omega A_\pm(\omega)]$ is expressed, depending on the presence of the CRTs and the A^2 term, as

$$\sigma_{\mathrm{CRA}}(\omega) = \begin{cases} \dfrac{\mathrm{i}ne^2}{m^*}\dfrac{1}{\omega-\omega_{\mathrm{c}}+\mathrm{i}0^+} & \text{(with } A^2 \text{ term)} \\ \dfrac{\mathrm{i}ne^2}{m^*}\dfrac{1}{\omega-\omega_{\mathrm{c}}+\mathrm{i}0^+}\dfrac{\omega_{\mathrm{c}}}{\omega} & \text{(without } A^2 \text{ term)} \end{cases} \tag{S60a}$$

$$\sigma_{\mathrm{CRI}}(\omega) = \begin{cases} \dfrac{\mathrm{i}ne^2}{m^*}\dfrac{1}{\omega+\omega_{\mathrm{c}}+\mathrm{i}0^+} & \text{(with CRTs and } A^2 \text{ term)} \\ \dfrac{\mathrm{i}ne^2}{m^*}\dfrac{-1}{\omega+\omega_{\mathrm{c}}+\mathrm{i}0^+}\dfrac{\omega_{\mathrm{c}}}{\omega} & \text{(with CRTs but without } A^2 \text{ term)} \\ \dfrac{\mathrm{i}ne^2}{m^*}\dfrac{1}{\omega+\mathrm{i}0^+} & \text{(without CRTs but with } A^2 \text{ term)} \\ 0 & \text{(without CRTs and } A^2 \text{ term)} \end{cases} \tag{S60b}$$

Then, the relative dielectric function $\varepsilon_\pm(\omega) = \varepsilon_{\mathrm{bg}} + \mathrm{i}\sigma_\pm(\omega)/(\varepsilon_0\omega d_{\mathrm{QW}})$ of the active layer is expressed as

$$\varepsilon_{\mathrm{CRA}}(\omega) = \begin{cases} \varepsilon_{\mathrm{bg}} - \dfrac{{\omega_{\mathrm{plasma}}}^2}{\omega(\omega-\omega_{\mathrm{c}}+\mathrm{i}0^+)} & \text{(with } A^2 \text{ term)} \\ \varepsilon_{\mathrm{bg}} - \dfrac{{\omega_{\mathrm{plasma}}}^2}{\omega(\omega-\omega_{\mathrm{c}}+\mathrm{i}0^+)}\dfrac{\omega_{\mathrm{c}}}{\omega} & \text{(without } A^2 \text{ term)} \end{cases} \tag{S61a}$$

$$\varepsilon_{\mathrm{CRI}}(\omega) = \begin{cases} \varepsilon_{\mathrm{bg}} - \dfrac{{\omega_{\mathrm{plasma}}}^2}{\omega(\omega+\omega_{\mathrm{c}}+\mathrm{i}0^+)} & \text{(with CRTs and } A^2 \text{ term)} \\ \varepsilon_{\mathrm{bg}} + \dfrac{{\omega_{\mathrm{plasma}}}^2}{\omega(\omega+\omega_{\mathrm{c}}+\mathrm{i}0^+)}\dfrac{\omega_{\mathrm{c}}}{\omega} & \text{(with CRTs but without } A^2 \text{ term)} \\ \varepsilon_{\mathrm{bg}} - \dfrac{{\omega_{\mathrm{plasma}}}^2}{\omega(\omega+\mathrm{i}0^+)} & \text{(without CRTs but with } A^2 \text{ term)} \\ \varepsilon_{\mathrm{bg}} & \text{(without CRTs and } A^2 \text{ term)} \end{cases} \tag{S61b}$$

Here, the plasma frequency is defined as

$${\omega_{\mathrm{plasma}}}^2 = \frac{e^2 n}{\varepsilon_0 m^* d_{\mathrm{QW}}} = \frac{2\varepsilon_{\mathrm{bg}} g_{n_z}^2}{|f_{n_z}(z_{\mathrm{2DEG}})|^2 d_{\mathrm{QW}}}. \tag{S62}$$

By using the above relative permittivities for that of the active layer, we can calculate the transmission spectra with/without the contributions from the CRTs and A^2 term. The CR decay rate is introduced by replacing $\mathrm{i}0^+$ with $\mathrm{i}\gamma$.

3.4 Effects of losses

While the CR decay rate γ appears to have been introduced phenomenologically at the end of the previous subsection, we can define it by using an appropriate quantum reservoir model. In this subsection, we describe the procedure, starting from the single-mode Hamiltonian given by Eq. (S43). First, let us introduce the dimensionless vector potential $\tilde{A}_\pm$, its conjugate momentum (electric field) $\tilde{\mathit{\Pi}}_\pm$, and electric current $\tilde{J}_\pm$ as

$$\tilde{A}_\pm \equiv \frac{\langle \hat{a}_\pm \rangle + \langle \hat{a}^\dagger_\mp \rangle}{\sqrt{2}} = \{\tilde{A}_\mp\}^*, \tag{S63a}$$

$$\tilde{\mathit{\Pi}}_\pm \equiv \frac{\langle \hat{a}_\pm \rangle - \langle \hat{a}^\dagger_\mp \rangle}{\mathrm{i}\sqrt{2}} = \{\tilde{\mathit{\Pi}}_\mp\}^*, \tag{S63b}$$

$$\tilde{J}_+ \equiv \langle \hat{b} \rangle + \frac{\mathrm{i}\sqrt{2}\bar{g}_1}{\omega_\mathrm{c}} \tilde{A}_+ = \{\tilde{J}_-\}^*, \tag{S63c}$$

$$\tilde{J}_- \equiv \langle \hat{b}^\dagger \rangle - \frac{\mathrm{i}\sqrt{2}\bar{g}_1}{\omega_\mathrm{c}} \tilde{A}_- = \{\tilde{J}_+\}^*. \tag{S63d}$$

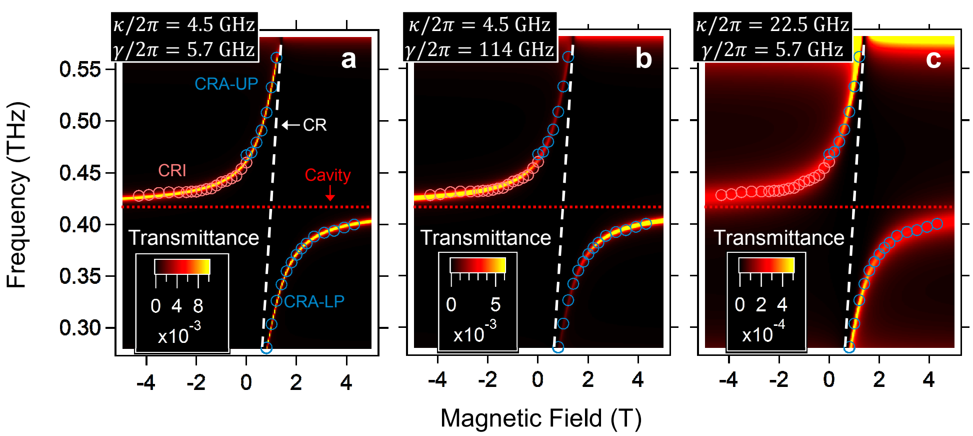

Figure S4: Semiclassical simulations of line brodening. **a**, Our experimental situation, where $\kappa/2\pi = 4.5$ GHz and $\gamma/2\pi = 5.7$ GHz. **b**, $\kappa/2\pi = 4.5$ GHz, $\gamma/2\pi = 114$ GHz. **c**, $\kappa/2\pi = 22.5$ GHz, $\gamma/2\pi = 5.7$ GHz. The colored circle markers denote the experimentally observed peak positions.

From the quantum Langevin equations derived from Eq. (S43) and the coupling with photonic and CR reservoirs [9], the equations of motion with losses are obtained as

$$\frac{\partial}{\partial t}\tilde{A}_{\pm} = \omega_{\rm cav}\tilde{\mathit{\Pi}}_{\pm}, \tag{S64a}$$

$$\frac{\partial}{\partial t}\tilde{\mathit{\Pi}}_{\pm} = -(\omega_{\rm cav} - {\rm i}\kappa)\tilde{A}_{\pm} \pm {\rm i}\sqrt{2}\bar{g}_1\tilde{J}_{\pm}, \tag{S64b}$$

$$\frac{\partial}{\partial t}\tilde{J}_{\pm} = (\mp{\rm i}\omega_{\rm c} - \gamma)\tilde{J}_{\pm} \pm \frac{{\rm i}\sqrt{2}\bar{g}_1\omega_{\rm cav}}{\omega_{\rm c}}\tilde{\mathit{\Pi}}_{\pm}. \tag{S64c}$$

Here, we introduced the CR decay rate γ for the electric current $\tilde{J}_{\pm}$ (electrons' velocity), not for the electrons' momentum ($\hat{b}$ and $\hat{b}^{\dagger}$). In the frequency domain, instead of Eq. (S44), these equations of motion reduce to the following equation for determining the three complex frequencies ω for the CRA-UP, CRA-LP, and CRI modes:

$$\omega^3 \mp (\omega_{\rm c} \mp {\rm i}\gamma)\omega^2 - \omega_{\rm cav}\left(\omega_{\rm cav} - {\rm i}\kappa + \frac{2\bar{g}_1{}^2}{\omega_{\rm c}}\right)\omega \pm (\omega_{\rm c} \mp {\rm i}\gamma)\omega_{\rm cav}(\omega_{\rm cav} - {\rm i}\kappa) = 0. \tag{S65}$$

The real and imaginary parts of ω represent, respectively, the resonance frequency and loss rate of a Landau-polariton mode. Further, this equation is transformed to the following dispersion relation:

$$\frac{\{\omega_{\rm cav}(\omega_{\rm cav} - {\rm i}\kappa)\}^{1/2}}{\omega} = \left\{1 - \frac{2g_1{}^2}{\omega(\omega \mp \omega_{\rm c} + {\rm i}\gamma)}\right\}^{1/2}. \tag{S66}$$

This equation replaces Eqs. (3) and (4) in the main text in the lossy case. On the left hand side, the photonic loss rate κ is introduced, while it is automatically incorporated in the semiclassical TMM simulations. The right hand side is the effective refractive index, and it corresponds to the square root of the dielectric permittivity used in the semiclassical simulations through Eqs. (S61) (with CRTs and A^2 terms) as

$$\frac{ck/\sqrt{\varepsilon_{\rm bg}}}{\omega} = \sqrt{\frac{\varepsilon_{\rm CRA/CRI}(\omega)}{\varepsilon_{\rm bg}}} = \sqrt{1 - \frac{2g_1{}^2}{\omega(\omega \mp \omega_{\rm c} + {\rm i}0^+)}\frac{L_1}{2d_{\rm QW}}}. \tag{S67}$$

Here, $ck/\sqrt{\varepsilon_{\rm bg}}$ corresponds to the cavity frequency when it is filled by a dielectric medium with $\varepsilon_{\rm bg}$. $L_1 = 2/|f_1(z_{\rm 2DEG})|^2$ is the effective cavity length, and the factor $L_1/(2d_{\rm QW})$ appeared due to the thin active layer (QWs) with a thickness of $d_{\rm QW}$ relative to the long effective cavity length L_1.

Therefore, in the presence of losses, the connection between the quantum theory and semiclassical simulation is well established. Below, we show results of the semiclassical simulations using different κ's and γ's.

Figure S4**a** shows the simulated transmission spectra using experimentally derived linewidth parameters, namely, $\kappa/2\pi = 4.5$ GHz and $\gamma/2\pi = 5.7$ GHz, showing nice agreement with experimental peak positions (colored circles). Then we simulated the case of $\kappa/2\pi = 4.5$ GHz and $\gamma/2\pi = 114$ GHz (Fig. S4**b**), where γ is increased by 20 times due to some CR line broadening effects, such as an increase in temperature. We see that, although the polariton line intensities become weaker when they move closer to the CR line, the frequencies remain unchanged. Furthermore, we increased $\kappa/2\pi$ to 22.5 GHz in Fig. S4**c**. Despite the broadening of polaritons in the vicinity of the cavity mode line, we again see no noticeable frequency mismatch between the calculation and experiment.

4 Asymptotic behavior of the CRA and CRI modes

A polaritonic gap has been previously observed by in similar Landau polariton systems [10, 11] . However, we find that, although a polaritonic gap indeed opens between the CRA-LP and CRA-UP branches as a result of ultrastrong coupling, the CRI mode completely closes it when B is sufficiently large. This point is evidenced by our simulations shown in Fig. S5. As B approaches $+\infty$ ($-\infty$), the CRA-LP mode (the CRI mode) asymptotically approaches the cavity frequency, and thus, there is no forbidden energy region in the dispersions.

5 Determining the values of κ and γ through semiclassical simulations

Although the bare photonic mode linewidth without a 2DEG was directly determined by THz transmission measurements (see Fig. 1**d** of the main text), the photon decay rate κ of the combined structure of the cavity and 2DEG still need to be determined separately using linewidth simulations, because the 2DEG introduces an additional background loss that increases κ. Similarly, γ also needs to go through the same procedure, because γ includes not only contributions from the DC scattering rate obtained from Hall mobility measurements but also the collective radiative decay (superradiance), which depends highly on the photonic environment of CR [12, 13].

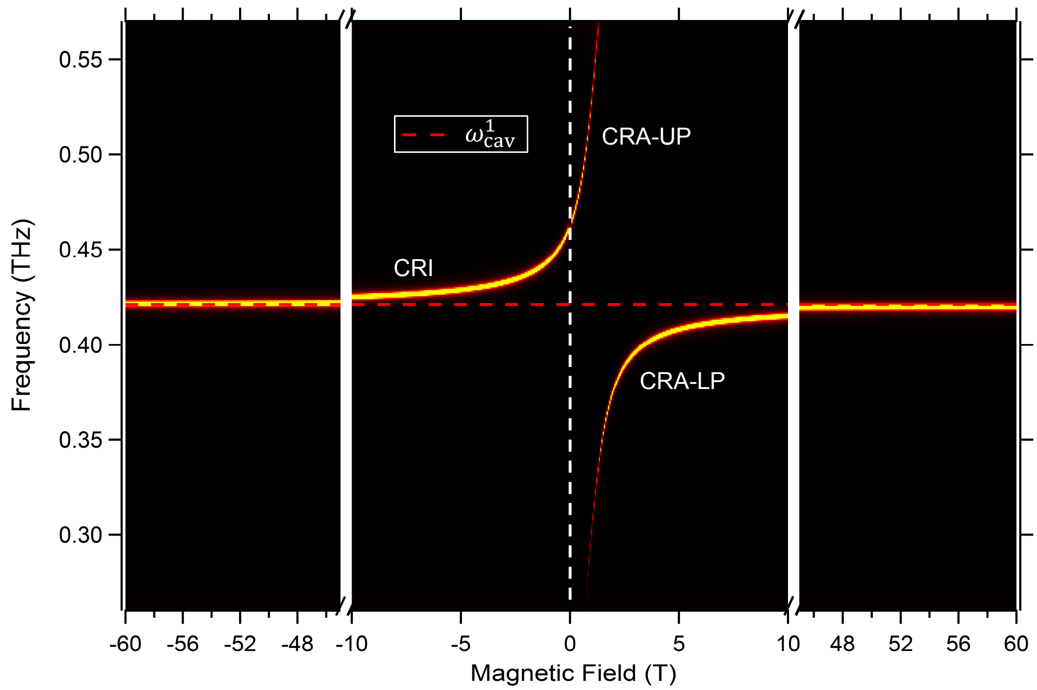

Figure S5: Simulated polariton dispersions up to $B = \pm 60$ T. The CRI and CRA-LP modes converge to ω_{cav}^1, closing the polaritonic gap.

Experimentally, we extracted the full-width-at-half-maximum (FWHM) of the zero detuning lower polariton (LP) and upper polariton (UP) peaks, and the FWHM of the CRI mode at 3 T. The lineshapes of the peaks chosen for fitting did not suffer from the minisplitting artifact (see Section 6). We introduced a finite imaginary part to the 2DEG background permittivity $\varepsilon_{\mathrm{bg}} = 3.6^2 + \alpha i$ to account for the photon loss induced by the 2DEG layer that affects κ. Here, α is a fitting parameter for adjustment. At a particular α (κ fixed), we continuously changed $\tau = 1/\gamma$ in Eq. (S6) and simulated the FWHMs of the LP and UP peaks at zero detuning, and the CRI peak at 3 T. As shown in Fig. S6, their results are plotted as a function of γ together with the corresponding κ value. We find that, when α is adjusted such that the corresponding $\kappa/2\pi$ value is 4.5 GHz, there is a value of $\gamma/2\pi = 5.7$ GHz, at which the simulated FWHMs of the LP, UP, and CRI mode agree best with the experimentally extracted values; see Fig. S6. We thus determined $\kappa/2\pi = 4.5$ GHz and $\gamma/2\pi = 5.7$ GHz, which are the numbers we used for calculating the cooperativity parameter.

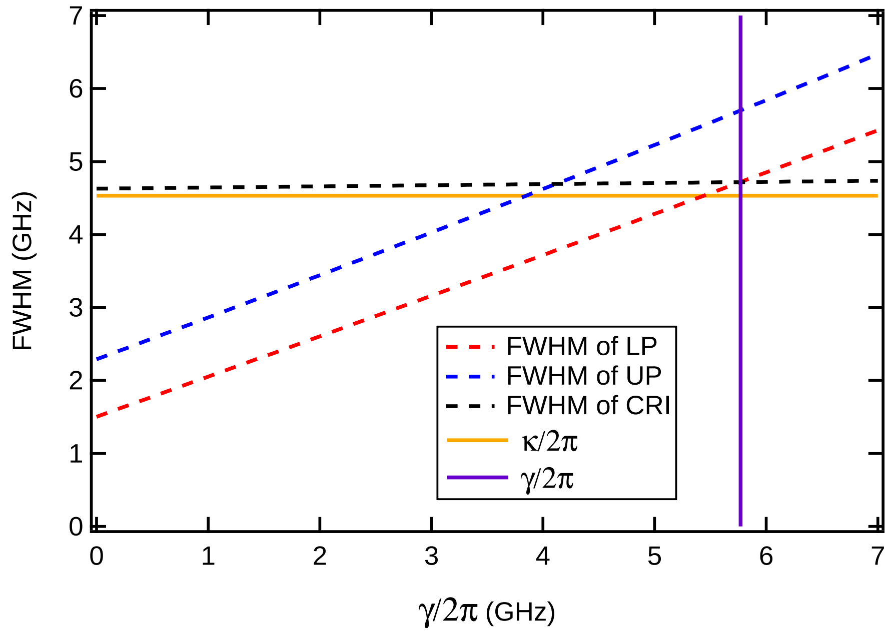

Figure S6: Linewidth simulations of first-order anticrossing using the transfer-matrix method. The solid horizontal and vertical lines indicate, respectively, the extracted κ and γ that can best fit the experimental polariton linewidths.

If we assume that the FWHM of the CRI mode at 3 T is equal to κ and that the FWHM of the LP and UP peaks at zero detuning are $(\kappa + \gamma)/2$, then we get $\kappa/2\pi = 4.8$ GHz and $\gamma/2\pi = 5.5$ GHz. The cooperativity parameter calculated with this choice of parameters is 3400, which does not differ very much from the current value (3513) obtained from the linewidth simulations. However, the linewidth simulation method we employed is still the most accurate way to determine κ and γ, because it automatically incorporates coupling effects between CR and transmission modes in photonic pass bands, as can be clearly seen in Fig. 3 in the main text.

6 Minisplittings in experimental spectra

In Fig. 2**a** in the main text, one can see several minisplitting features appearing in all polariton branches. Here we demonstrate that these features arise from a

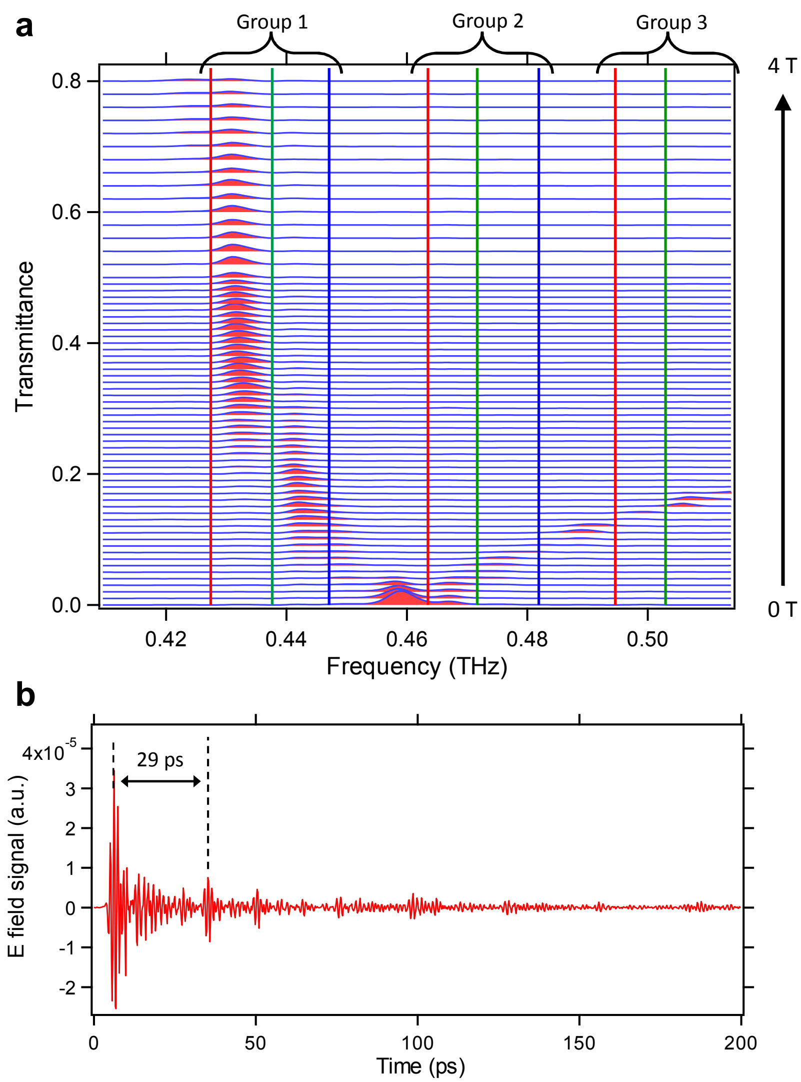

Figure S7: **a**, Experimental transmittance spectra from 0 T to 4 T. Center frequencies of minisplitting features are indicated by solid vertical colored lines. **b**, Typical time-domain signal for a THz wave transmitted through the cavity sample. The major back-reflection pulse appears 29 ps after the main pulse.

transmission modulation effect due to cryostat window back-reflections.

In Fig. S7**a**, we plot transmittance spectra near the CRI mode and CRA-UP mode frequencies in a magnetic field range of 0 to 4 T. Minisplitting features can be identified clearly, the center frequency of each of which was determined and is indicated by a vertical colored line in the figure. As described in the Materials and Methods section, frequency-domain spectra are obtained by Fourier transforming time-domain electric field oscillations; see Fig. S7**b** for a typical THz waveform transmitted through a cavity sample. Oscillation signals from 0 ps to 28 ps are due to multiple reflections within the cavity silicon Bragg mirrors, which is purely useful information we need. At 29 ps, a replica pulse appears, and by directly comparing it with the THz signal passing through an aperture in the cryostat, we confirmed that this replica pulse comes from THz back-reflections within the cryostat cold windows. Pulses that are separate in time are described as Febry-Perot resonances in the frequency domain. They show up as equal-frequency-spaced transmission modulations across the entire spectrum. From the time separation of 29 ps between the main pulse and major back-reflection pulse, we estimate the interval between major transmission modulations in the frequency domain to be 34 GHz.

We found that the colored vertical lines in Fig. S7**a** show such a periodic behavior. If we define a group of lines consisting of one red line, one green line, and one blue line, we can find replicas of such a group in the frequency spectrum, separated apart from each other by 34 GHz. The first group appears in the CRI branch. The second and third groups appear in the CRA-UP branch. The reason why multiple lines exist in one group is because of back-reflections from other optical elements in the beam path, whose Febry-Perot transmission modulations are superimposed on the main modulation with a frequency interval of 34 GHz. From this analysis, we determined the cause of minisplitting features to be most likely due to back-reflection signal artifacts, rather than from light-matter coupling.

The minisplitting features can affect the determination of polariton peak frequencies in Figs. 3 and 4 in the main text. Hence, in the vicinity of a minisplitting, we took a weighted average of the frequencies of the two peaks, taking into account their respective spectral weights.

7 Circularly polarized THz spectroscopy

Figure 2**e** in the main text demonstrates the polarization selection rules of the polaritons lines. For a fixed right-hand circularly polarized probe beam, we exclusively observed the VRS (vacuum BS shift) at positive (negative) B fields. Here, we show the details of our circular polarization resolved THz spectroscopy exper-

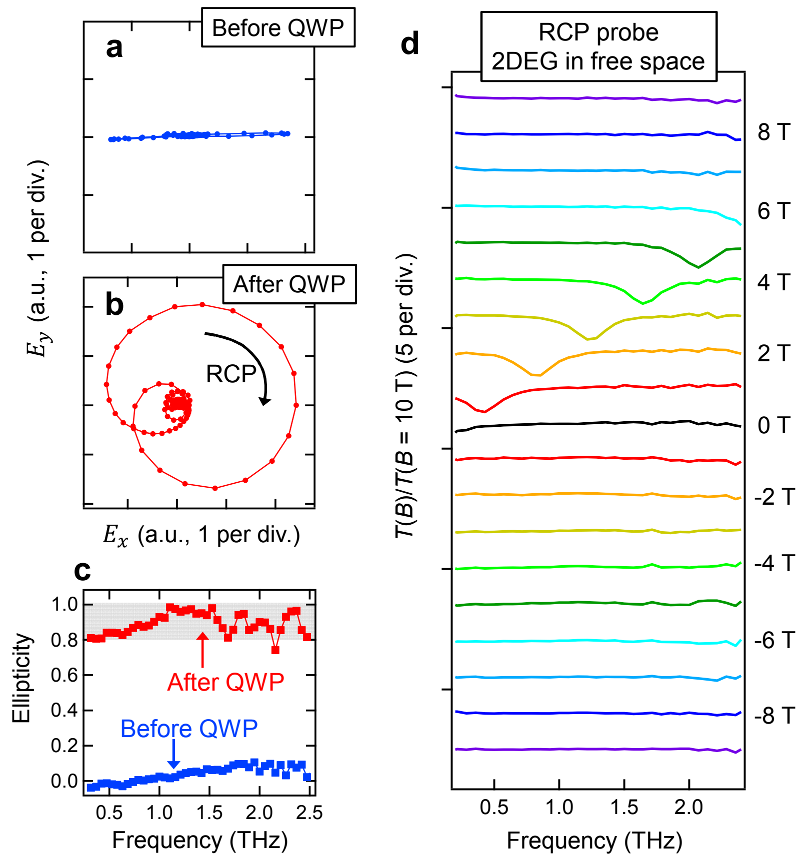

Figure S8: The THz electric field E_y plotted versus E_x **a**, before and **b**, after the beam passes through the THz QWP. A clear conversion from linear to circular polarization can be observed. **c**, Ellipticity spectra of the THz field shown in **a** and **b**. **d**, Transmittance spectra of a 2DEG in free space probed by the RCP THz light at various magnetic fields. Curves are offset for clarity.

iments.

We converted our linearly polarized THz probe beam into a right-hand circularly polarized (RCP) beam by using an achromatic THz quarter wave plate (QWP). The wave plate adopted a multi-stacked prism-type geometry. It controls the phase retardation of the two orthogonal THz electric igfield components through multiple total-internal reflections within the prism [14]. Figure S8**a** and

b show the time-domain THz electric field E_y plotted versus E_x, manifesting the THz polarization states before and after the beam passes through the QWP, respectively. Here, the x-y plane is the plane normal to the propagation direction. Before passing through the QWP, the THz field is in a linearly x-polarized state, while the electric field clearly engages in a circular motion in the x-y plane after passing through the QWP. The handedness of the motion suggests that the beam has become mostly RCP. In order to quantitatively describe the polarization state, we calculated the ellipticity spectra of the THz fields plotted in Fig. S8**a** and **b**. The results are shown in Fig. S8**c**. After the beam passes through the QWP, the ellipticity of the entire THz frequency bandwidth falls above 0.8, suggesting excellent purity of the RCP light in the beam; note that an ellipticity of one means that the beam is perfectly RCP. A broadband THz QWP with such an ideal response has never been used in condensed matter physics experiments.

As shown in Fig. S8**d**, we measured the transmittance of a 2DEG in free space using the RCP THz probe. The 2DEG sample and measurement temperature were the same as those in Fig. 1**e** in the main text. The spectrum at $B = 10$ T was used as the reference. We observed clear CR absorption features at positive B fields, corresponding to the resonant absorption of the CRA mode. However, in the negative B region, we observed no response, because the electrons rotate in the opposite direction to the RCP light. This confirms that the electrons do not interact with the CRI mode of radiation in free space. This result is in sharp contrast to the data obtained from measurements on the 2DEG-cavity sample shown in Fig. 2**e** in the main text, where the CRI mode frequency shift unambiguously evidences the counter-rotating light-matter interaction in the USC regime.

8 Comparison with the valley-exclusive BS shift observed in monolayer WS_2 [15]

The vacuum BS shift can be viewed as a state repulsion between the CR line in the negative B region and the cavity mode line. This view is schematically depicted in Fig. 1**b** in the main text. The coupling between the cavity mode (dashed black line) and the CR line in the negative B region (dashed blue line) leads to an energy splitting of the left-hand circularly polarized (LCP) light (solid blue lines). The upper polariton continuously extends to the positive B region and becomes the CRI mode in the spectra shown in Fig. 2**a** in the main text. The red-shift of this CRI mode in the positive B region is the vacuum BS shift.

In our system, CR in the positive and negative B regions can be viewed as a time-reversed pair; similarly, the vacuum Rabi splitting (VRS) and vacuum BS shift phenomena can be considered to be time-reversed partners. Such a unique setup allowed us to use another pair of time-reversed probes, namely, RCP and LCP THz radiation, to unambiguously observe the VRS and vacuum BS shift, respectively. As depicted in Fig. S9, RCP (LCP) radiation probes the VRS (vacuum BS shift) by exciting CR at a positive (negative) B field and probes the vacuum BS shift (VRS) by exciting CR at a negative (positive) B field. We notice that our design has some similarities to the work by E. Sie *et al.* [15]. As shown in Fig. S9, the K and K' valleys of WS_2 in Ref. [15] were the time-reversed matter transitions. The authors used a circularly polarized pump field to induce an optical Stark shift (OSS) and a dynamical BS shift in separate valleys.

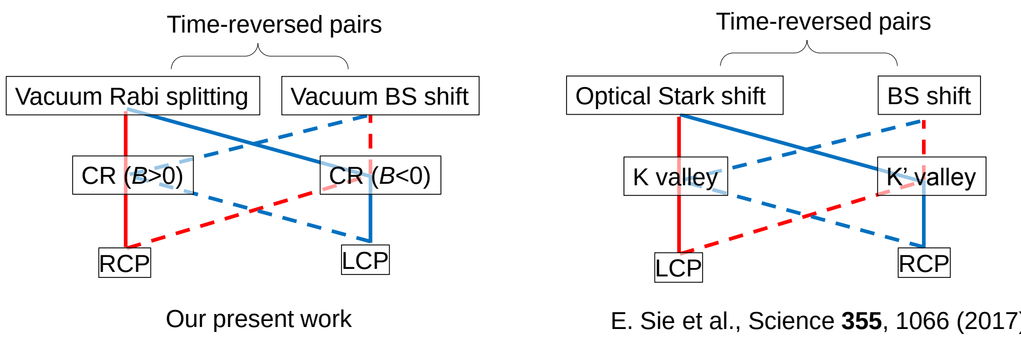

Figure S9: Diagram showing how time-reversed physical phenomena, matter excitations, and light fields are correlated. Our work possesses an analogous scheme to Ref. [15]. The solid and dashed lines indicate the co-rotating and counter-rotating couplings, respectively.

Furthermore, we constructed an energy level scheme for the system in Ref. [15] in a fashion similar to our Fig. 1**b** in the main text. Through a detailed comparison between the two analogous systems, we found that our vacuum BS shift has an opposite sign to the BS shift in Ref. [15]. The reason is the different definitions of the energy zero.

Figures S10**a** and **b** show the schemes to identify the vacuum BS shift in our work and the BS shift in Ref. [15], respectively. The vertical red and blue arrows mark the frequency differences between a polariton line and a reference line. Red (blue) arrows denote negative (positive) frequency shifts. In our system, because of our capability to clearly separate the contributions from the CRTs and the A^2

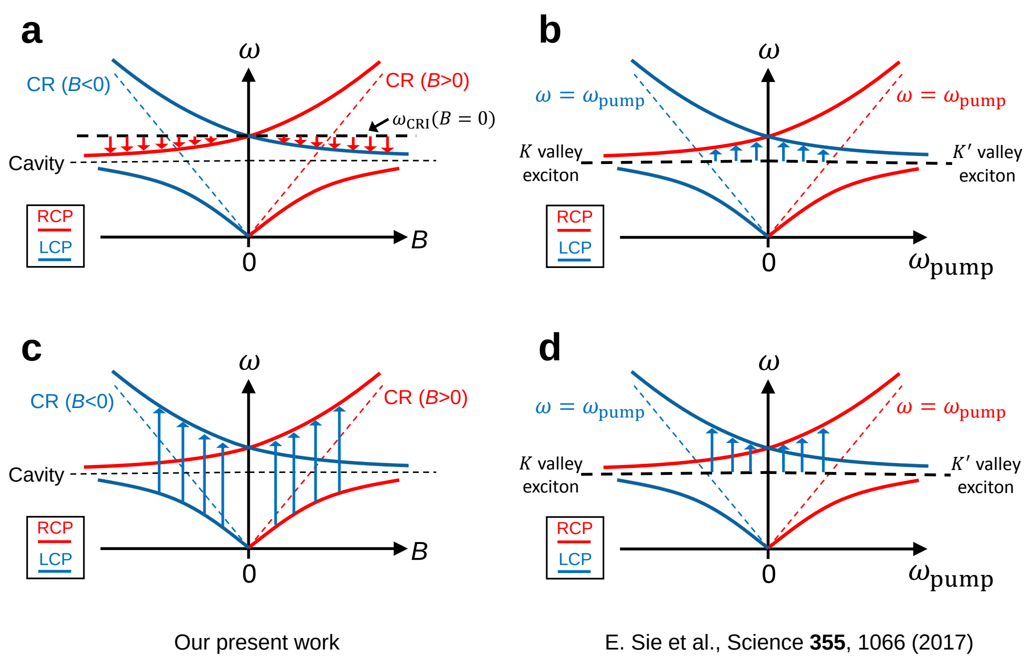

Figure S10: **Energy level schemes showing various features observed in our work and in Ref. [15].** Vertical red and blue arrows mark the frequency shifts that can be identified as **a**, the vacuum BS shift in our work, **b**, the BS shift in Ref. [15], **c**, the VRS in our work, and **d**, the OSS in Ref. [15]. Red (blue) arrows indicate negative (positive) shifts.

terms, we identified that the deviation of the CRI mode and the cavity mode is due to the A^2 terms. Therefore, when we extract the vacuum BS shift values, we tried to identify what additional frequency shift the CRTs induce on top of the shift due to the A^2 terms; the energy zero for the vacuum BS shift is then defined as $\omega_{\rm CRI}(B=0)$. This leads to a negative vacuum BS shift (red arrows in Fig. S10**a**). On the other hand, for the BS shift observed in Ref. [15], the energy zero is defined as the exciton energy, so the BS shift is always positive (blue arrows in Fig. S10**b**); the magnitude of the BS shift decreases when the detuning becomes smaller, which is consistent with the results in Ref. [15].

Furthermore, we extracted the frequency shift of the CRI branch, assuming that the energy zero is defined to be the cavity mode frequency, namely, $\omega_{\rm CRI}(B)-\omega_{\rm cav}$, and plotted it in a similar way to Ref. [15] as a function of $1/(\omega_{\rm cav}+\omega_{\rm c})$. In

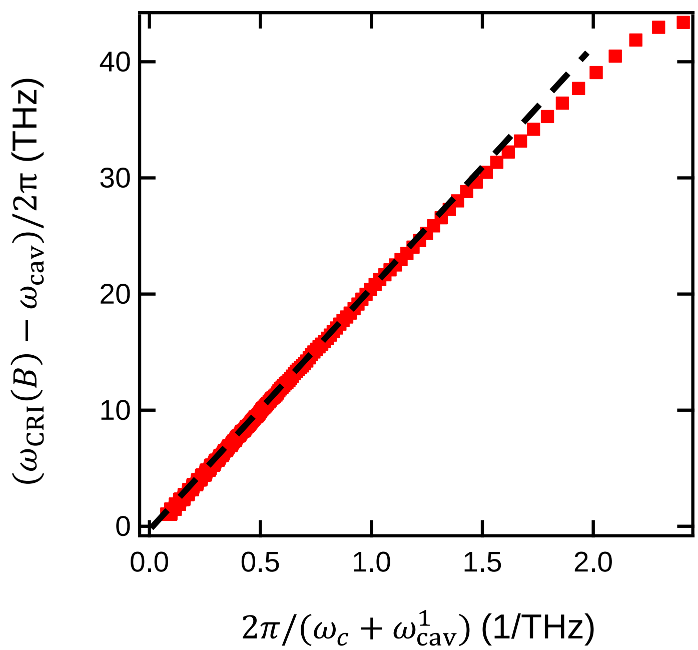

Figure S11: Frequency scaling law of the vacuum BS shift.

the large detuning region, they should show a linear relationship. As shown in Fig. S11, such a relationship is confirmed. Deviation from the linear behavior starts to appear when $1/(\omega_{\mathrm{cav}} + \omega_{\mathrm{c}})$ becomes larger.

For a more complete comparison, the schemes to identify the VRS in our work and the OSS in Ref. [15] are depicted in Figs. S10**c** and **d**, respectively. The VRS is the frequency splitting between the UP and LP, while the OSS can be understood as the frequency blue-shift of the UP relative to the exciton line under a subbandgap circularly polarized optical pump field.

References

[1] S. Birner, *et al.*, *IEEE Trans. Electron. Dev.* **54**, 2137 (2007).

[2] J. Hao, L. Zhou, *Phys. Rev. B* **77**, 094201 (2008).

[3] C. Cohen-Tannoudji, J. Dupont-Roc, G. Grynberg, *Photons and Atoms: Introduction to Quantum Electrodynamics* (John Wiley & Sons, Inc., New York, 1989).

[4] L. Knöll, S. Scheel, D.-G. Welsch, *Coherence and Statistics of Photons and Atoms*, J. Peřina, ed., Wiley Series in Lasers and Applications (Wiley, New York, 2001), chap. 1, pp. 1–64.

[5] W. Kohn, *Phys. Rev.* **123**, 1242 (1961).

[6] D. Yoshioka, *The Quantum Hall Effect* (Springer, Berlin and New York, 2002).

[7] R. J. Glauber, M. Lewenstein, *Phys. Rev. A* **43**, 467 (1991).

[8] S. Huant, A. Mandray, B. Etienne, *Phys. Rev. B* **46**, 2613 (1992).

[9] M. Bamba, N. Imoto, *Phys. Rev. A* **94**, 033802 (2016).

[10] C. Maissen, *et al.*, *Phys. Rev. B* **90**, 205309 (2014).

[11] C. Maissen, G. Scalari, M. Beck, J. Faist, *New J. Phys.* **19**, 043022 (2017).

[12] Q. Zhang, *et al.*, *Phys. Rev. Lett.* **113**, 047601 (2014).

[13] Q. Zhang, *et al.*, *Nat. Phys.* **12**, 1005 (2016).

[14] Y. Kawada, *et al.*, *Opt. Lett.* **39**, 2794 (2014).

[15] E. J. Sie, *et al.*, *Science* **355**, 1066 (2017).